Directional Breaking Kinematics Observations from 3D Stereo Reconstruction of Ocean Waves

Bernard Akaawase[1], Leonel Romero[1], Alvise Benetazzo[2]

[1]Department of Marine Sciences, University of Connecticut, Groton, CT, USA

[2]Istituto di Scienze Marine (ISMAR), Consiglio Nazionale delle Ricerche (CNR), Venice, Italy

Key Points:

- The directionality of wave-breaking and wave energy spectrum is investigated via stereo visible imagery.
- The energy spectrum is bi-modal whereas the breakers are unimodal with more breaking occurring in the dominant waves/wind direction.
- The observed distribution of wave-breaking crest lengths is azimuthally much narrower than the wave spectrum.

Corresponding author: Bernard Akaawase, bernard.akaawase@uconn.edu

Abstract

Short ocean surface waves are important for remote sensing, air-sea exchange, and underwater acoustics. The energy spectrum at scales much shorter than the dominant waves are azimuthally bimodal. However, widely used wave models fail to reproduce the bimodality of the short gravity waves. Recent studies have shown that an azimuthally narrow dissipation due to breaking can significantly improve model performance. Thus, highlighting the importance of the directional energy balance of wave models. We utilized stereo visible imagery to quantify the directional wave-breaking kinematics and compare them against the energy spectrum and different dissipation parameterizations and model solutions. The results show that wave-breaking is azimuthally unimodal and narrower than the bimodal energy spectrum, suggesting that wave-breaking dissipation combines with the nonlinear energy fluxes due to wave-wave interactions to yield enhanced bimodality. The findings are useful for constraining energy dissipation parameterizations for spectral wave models and improved understanding of air-sea fluxes.

Plain Language Summary

Short gravity waves on the ocean surface play crucial roles in remote sensing, air-sea exchange, and underwater acoustics. Despite their significance, widely used wave models fail to accurately reproduce the directionality of short gravity waves. This study investigates the relationship between the directional distribution of wave breaking and the energy spectrum as recent studies have suggested that such knowledge is vital for improved wave model performance. Utilizing stereo visible imagery and three-dimensional reconstruction of the sea surface elevation, we show that the energy spectrum exhibits strong azimuthal bimodality away from the spectral peak, while the statistics of wave breaking is unimodal and much narrower. This supports recent modeling efforts that demonstrate that a directionally narrow breaking dissipation can significantly improve the performance of spectral wave models. The results presented are useful for optimization and constraining dissipation parameterizations due to breaking for spectral wave models, and improving understanding of air-sea exchange processes.

1 Introduction

Several processes within the oceanic and atmospheric boundary layers are modulated by surface wave breaking. These include the development of the wave field (Melville,

1996), momentum transfer from the surface waves to currents (Pizzo et al., 2016; Romero, 2019), and air-sea fluxes (Deike & Melville, 2018; Shin et al., 2022; Deike, 2022). Wave-breaking is also a source of the near-surface turbulent kinetic energy and underwater sound generation (Gemmrich et al., 2008). Despite the significant impact of wave-breaking, it is poorly understood. Much of the present knowledge about wave breaking has emerged from field observations, laboratory and numerical experiments (Monahan & Muircheartaigh, 1980; Duncan, 1981; Phillips, 1985; M. L. Banner et al., 2000, 2002; Drazen et al., 2008; Callaghan et al., 2008; Gemmrich et al., 2008; Kleiss & Melville, 2010; Romero et al., 2012; Derakhti et al., 2020; Sutherland & Melville, 2013; Wu et al., 2022; Thomson, 2012). In this study, we investigate wave breaking using three-dimensional stereo reconstruction of the sea surface from visible imagery.

Phillips (1985) introduced a statistical approach for investigating wave-breaking, the $\Lambda(c)$ distribution, which is the expected length of breaking fronts advancing with speeds c to $c+dc$ per unit surface area. The moments of $\Lambda(c)$ correspond to various physical parameters. The first five moments (in order 1-5) are related to the fraction of the sea surface overturned by wave-breaking per unit time, the fractional area of the sea surface occupied by the actively breaking waves, the entrained air per unit area per time, the momentum transferred per unit area, and the energy dissipation per unit area (Phillips, 1985; Melville & Matusov, 2002; Kleiss & Melville, 2010; Deike et al., 2017; Romero, 2019). Previous studies have quantified $\Lambda(c)$ using sea spikes from radar backscatter, bubble signatures in visible-imagery, and temperature structures in infrared-imagery (Melville & Matusov, 2002; Phillips et al., 2001; Jessup & Phadnis, 2005; Gemmrich et al., 2008; Kleiss & Melville, 2010; Zappa et al., 2012; Sutherland & Melville, 2013; Romero et al., 2017). Although numerous measurements of $\Lambda(c)$ exist, only few have considered the direction of wave-breaking (Melville & Matusov, 2002; Gemmrich et al., 2008; Kleiss & Melville, 2011). To the best of our knowledge, no study has compared the directionality of wave-breaking to the energy spectrum. Such information is crucial as recent studies suggest that the directionality of the dissipation due to wave-breaking can have important implications for the dynamics that shape the wave spectrum (Romero & Lubana, 2022; Alday & Ardhuin, 2023). Hence, the need for a more detailed examination of breaking directionality for different environmental conditions.

In deep water, the evolution of energy spectrum $F(k,\theta)$ can be described by radiative transfer equation

$$\frac{\partial F(k,\theta)}{\partial t} + \mathbf{c}_g \cdot \nabla F(k,\theta) = S_{in} + S_{nl} + S_{ds}, \tag{1}$$

where the left-hand-side is the time derivative and advection at the group velocity, and the source terms on the right right-hand-side are the wind input S_{in} necessary for wave growth, the nonlinear interactions S_{nl}, and dissipation S_{ds}. To leading order, S_{nl} controls the spectral shape of short waves (M. S. Longuet-Higgins, 1976; M. Banner & Young, 1994; Toffoli et al., 2010). It is well established that $F(k,\theta)$ is unimodal at the spectral peak and becomes bimodal at lower and higher wavenumbers (I. Young et al., 1995; Ewans, 1998; Hwang et al., 2000; Romero & Melville, 2010a; Leckler et al., 2015; Peureux et al., 2018) with the lobe separation approaching $\pm 90^o$ at higher wavenumbers (Lenain & Melville, 2017). However, efforts to model the directional spectrum with the 'exact' computations of S_{nl} systematically yielded narrower spectra and weak bimodality at high wavenumbers compared to observations (Romero & Melville, 2010b; Liu et al., 2019; Romero & Lubana, 2022).

Following the work of Donelan (2001) on nonlinear breaking dissipation due to long wave-short wave modulation (M. Longuet-Higgins & Stewart, 1960; M. Longuet-Higgins, 1987; Guimarães, 2018; Peureux et al., 2018, 2021; Dulov et al., 2021), Romero (2019) developed a breaking parametrization much narrower than the energy spectrum, allowing numerical solutions with 'exact' computations of S_{nl} to yield enhanced bimodality consistent with observations. Here, we further assess the Romero (2019) wave-breaking model against field measurements of wave-breaking kinematics and energy spectrum. The paper is organized as follows. Section 2 describes the data set and explicitly documents how the visible images are processed to obtain the sea surface elevation and the statistics of wave-breaking kinematics. The results are presented in Section 3, followed by discussion and conclusions in Section 4.

2 Data and Methods

2.1 Data Description

We analyzed an existing dataset of stereo visible imagery, which was used to obtain 3D space-time sea surface elevation fields $\eta(x,y,t)$, where t denotes time, x and y are the world coordinates (see Figure S2). The data was collected in 2015 at the Acqua

Alta (AA) oceanographic research tower `https://www.ismar.cnr.it/en/infrastructures/oceanographic-infrastructures/acqua-alta-tower` (Benetazzo et al., 2012), located 15km offshore of Venice in the northern Adriatic Sea (Italy; 45.32^{o}N, 12.51^{o}E) where the water depth is 17m. The stereo setup consisted of two 5 MP (2048×2456) synchronized BM-500GE JAI cameras equipped with 5 mm low distortion lenses. The stereo system was mounted at 12.5 m above sea level with a baseline of 2.5 m, and a grazing angle of 25^o from the horizontal. The data was acquired for 30 minutes at 12 Hz (corresponding to 21570 frames) in conditions of relatively steady winds from the East-North-East averaging 13ms^{-1} at the standard 10m reference level (U_{10}), see wind time series in Figure S1. The significant wave height (H_s) was 1.99 m, the peak period (T_p) 6.5 s, and the corresponding wave age $c_p/U_{10} = 0.8$ as determined from the linear dispersion relationship. In addition, the peak wave direction was aligned with the wind. See Guimarães et al. (2020) for detailed description of the dataset (AA02).

2.2 Three Dimensional (3D) Reconstruction of the Ocean Waves

Ocean waves can be measured with instruments that solely provide the time series of the sea surface elevation (either in Eulerian or Lagrangian frame) $\eta(t)$, or in two-dimension (2D) with arrays of wave gauges to obtain limited space but robust time information. Alternatively, radar-based systems, scanning lidars, and computer vision or 'stereography' can be used to obtain 2D measurements with higher directional resolution (M. Banner et al., 1989; I. Young et al., 1995; Jasper et al., 2020; Hwang et al., 2000, 2000; Romero & Melville, 2010a; Lenain & Melville, 2017; Benetazzo, 2006). One of the first applications of stereography in oceanographic research involved computing the directional spectra of ocean waves from 3D elevation maps measured off San Diego from an offshore tower (M. Banner et al., 1989). Since then, this approach has been used to study surface wave processes. In this work, we utilized the Wave Acquisition Stereo System (WASS) pipeline '`https://sites.google.com/unive.it/wass/home/`', an open-source package that efficiently reconstructs ocean surface waves in 3D (Benetazzo, 2006; Benetazzo et al., 2012; Bergamasco et al., 2017). The technique can provide measurements that allow for the calculation of wave-breaking kinematics and the computation of unambiguous directional wave energy spectrum coincidentally, making it suitable for investigating short waves which are broadly distributed in azimuth spanning over ±80^o

(Peureux et al., 2018). A detailed description of WASS is provided in the supporting information.

2.3 Wave Spectral Analysis

WASS can capture the wave crests within its field of view but cannot resolve the wave troughs that are far from the cameras due to shadowing from the crests. Moreover, the spatial resolution and the quantization errors become larger with increasing distance from the cameras (Benetazzo et al., 2018). This motivated us to use a multi-window approach comprised of a large trapezoidal-window that adaptively follows the shape of the WASS swath and a small square-window. The larger window resolves the low wavenumbers, while the smaller window does a better job resolving the shorter waves. The trapezoidal-shaped swath is typical for grazing angle deployment when the video reconstruction is presented in a local cartesian frame (see Figure S2a).

Before computing the spectra, the data in the small-window was spatially detrended, and both windows were Hann-tapered around the edges. The tapering of the larger-window was performed adaptively to follow the data swath (Romero & Melville, 2010a), as demonstrated in Figure S2. Each window was zero-padded to thrice its initial size. The 2D wavenumber spectrum $F(k_x, k_y)$ was computed unambiguously from the 3D space-time Fast Fourier Transform of the wave field $\eta(x, y, t)$ by integrating all the positive frequencies and multiplying the spectrum by a factor of two to take care of the energy loss due to the negative frequencies according to

$$F(k_x, k_y) = 2 \int_0^{\omega_{max}} F(k_x, k_y, \omega) d\omega, \tag{2}$$

where $F(k_x, k_y, \omega)$ is the 3D spectrum. The directional spectrum was converted from cartesian to polar coordinates of components

$$\begin{aligned} k_x &= k \cos\theta \\ k_y &= k \sin\theta \end{aligned} \tag{3}$$

such that the variance of the sea surface elevation $\langle \eta^2 \rangle$ is preserved according to

$$\langle \eta^2 \rangle = \int \int F(k\cos\theta,\, k\sin\theta)\, k\, dk\, d\theta = \int \int F(k_x, k_y)\, dk_x\, dk_y, \tag{4}$$

where k is the value of the Jacobian determinant $J = \left|\frac{\partial(k_y, k_x)}{\partial(k, \theta)}\right|$ as given by

$$J = \begin{vmatrix} \frac{\partial k_x}{\partial k} & \frac{\partial k_x}{\partial \theta} \\ \frac{\partial k_y}{\partial k} & \frac{\partial k_y}{\partial \theta} \end{vmatrix} = \begin{vmatrix} \cos\theta & -k\sin\theta \\ \sin\theta & k\cos\theta \end{vmatrix} = k(\sin^2\theta + \cos^2\theta) = k. \tag{5}$$

Here we refer to $F(k\cos\theta,\, k\sin\theta)$ as $F(k, \theta)$ following the convention used in certain studies (M. L. Banner, 1990; Hwang et al., 2000; Romero et al., 2012; Romero, 2019; Romero & Lubana, 2022). But note that the 'true' polar spectrum is defined as $E(k, \theta) = F(k_x, k_y)J$ such that $\langle \eta^2 \rangle = \int\int E(k, \theta)\, dk\, d\theta$ (Tolman et al., 2009; Holthuijsen, 2010; Benetazzo et al., 2016; Peureux et al., 2018).

The spectrum from each of the windows was calibrated with its respective variances and the resulting spectra (small and large windows) were then blended through ramp functions

$$\Gamma_1 = 1 - \tanh\left(\frac{2\mathrm{k}}{\mathrm{k_o}}\right)^8 \tag{6}$$

and $\Gamma_2 = 1 - \Gamma_1$, where k_o=0.9 radm^{-1} is the transition wavenumber (Romero et al., 2019). After applying the ramp functions, the merged 2D spectrum is simply an element-wise sum of the two spectra. Following I. Young (1995), the peak wavenumber k_p and peak wave direction θ_p were computed through weighted integrals of the spectrum to the fourth power according to

$$k_p = \frac{\int\int F(k, \theta)^4 k^2 dk d\theta}{\int\int F(k, \theta)^4 k dk d\theta}, \tag{7}$$

and

$$\theta_p = \arctan\left(\frac{\int\int F(k, \theta)^4 \sin\theta k dk d\theta}{\int\int F(k, \theta)^4 \cos\theta k dk d\theta}\right). \tag{8}$$

2.4 Wave Breaking Kinematics Computations

Previous field experiments have employed different techniques to determine $\Lambda(c)$. The existing techniques can be categorized into event-based, temporal, or elemental. The event-based approach assigns a single speed to an entire breaking event, and the crest length is obtained by summing all crest lengths measured during the evolution of that breaking event (Gemmrich et al., 2008). The temporal method extracts a single speed from each breaking front per snapshot, along with the total crest lengths (Jessup & Phadnis, 2005). While the elemental approach considers individual points along the actively breaking fronts to determine the speed and the crest length (Melville & Matusov, 2002;

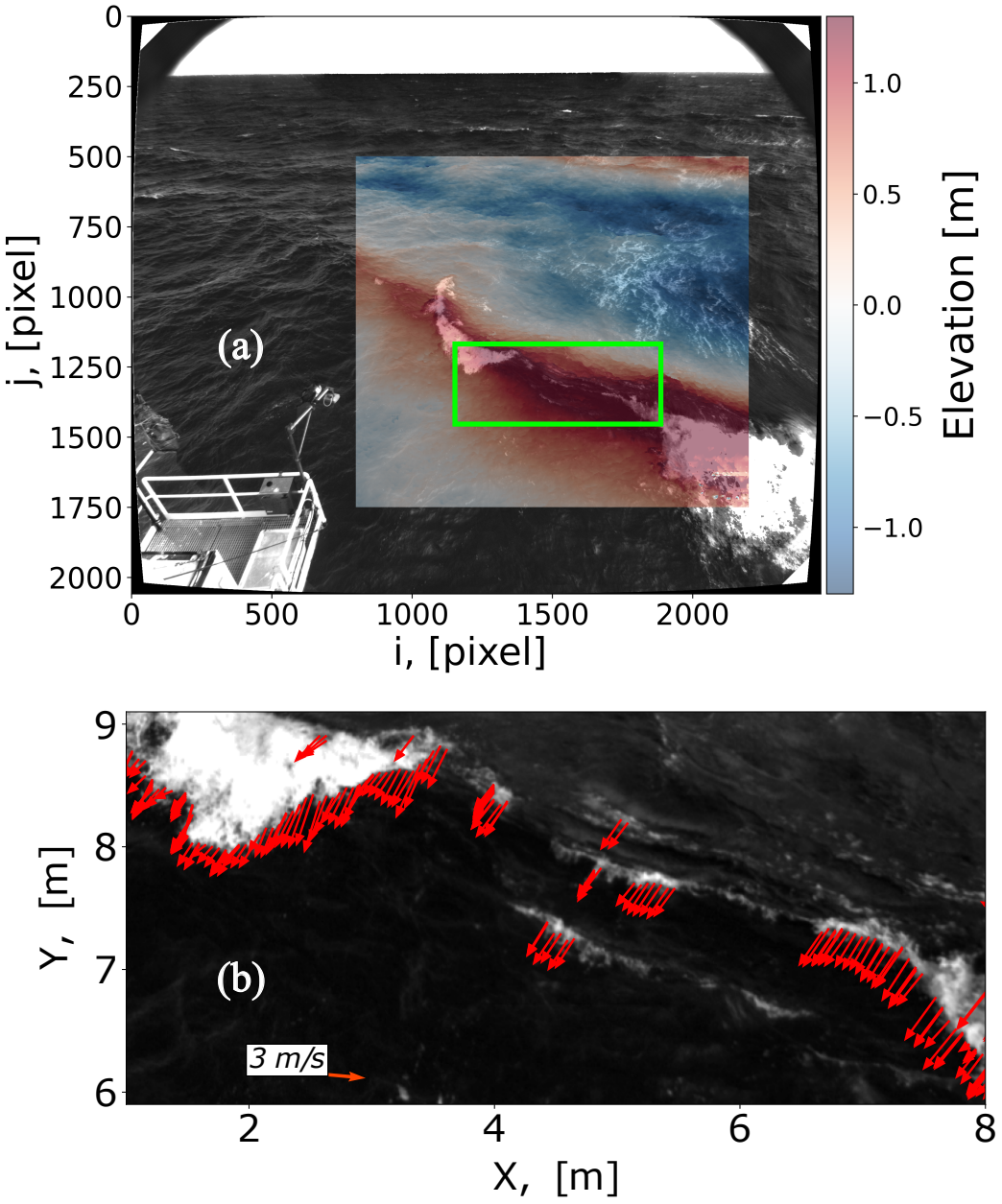

Figure 1. (a) Example of the sea surface elevation reconstructed with the WASS pipeline and (b) snapshot of detected breaker also indicated with a green box in (a). The green box corresponds to the analysis region used to compute the breaking kinematics statistics. The red arrows show the estimated velocities along the wave-breaking fronts.

Kleiss & Melville, 2011). Here, we adopt the elemental approach to calculate the kinematics of air-entraining breakers following the techniques developed by Kleiss and Melville (2011) and Sutherland and Melville (2013), which involves detecting wave-breaking via a brightness threshold and tracking the actively breaking events between frames. Refer to the supporting information for a detailed description. The tracked fronts are then converted to physical units using the WASS information as described below.

During the course of this work, we identified occasional motion of the cameras based on visual inspection of the imagery over the portion of the AA-tower in the images (Figure 1a). We corrected for camera motion between consecutive stereo image pair using control points over the AA-tower and near the horizon. Therefore the entire analysis of the wave-breaking kinematics was carried through consecutive stereo image pairs. The extrinsic parameters obtained from the first stereo image pair was also used for consecutive pair during the 3D reconstruction. We further assessed camera motion errors through the difference of the mean sea level between consecutive frames, which gave a median deviation of 2cm. Consecutive frames that had mean elevation differences greater than 3 median deviations ($\pm$ 6cm) were considered 'shaky' and excluded from the analysis, which were only about 5% of the data. Figure S4 compares time series of mean elevation differences between consecutive frames of the corrected and raw images showing significant improvement. We also limited our analysis to the image area closest to the camera, where troughs are not shadowed by crests.

The WASS information was used to convert the PIV pixel-vectors $(\Delta i, \Delta j)$ computed from a pair of images collected at time t and $t+\Delta t$ into physical displacements $(\Delta x, \Delta y)$ according to

$$\begin{aligned} \Delta x &= x(t+\Delta t\,|i,j) - x(t\,|i-\Delta i, j-\Delta j), \\ \Delta y &= y(t+\Delta t\,|i,j) - y(t\,|i-\Delta i, j-\Delta j). \end{aligned} \tag{9}$$

where $x(t,i,j)$ and $y(t,i,j)$ are the horizontal coordinates along the mean sea plane projected on to the image coordinates i, j. And the corresponding velocities are given by

$$\begin{aligned} c_x &= \frac{\Delta x}{\Delta t}, \\ c_y &= \frac{\Delta y}{\Delta t}. \end{aligned} \tag{10}$$

We used consecutive images so that $\Delta t = 1/f_s$, with f_s corresponding to the sampling frequency. The resulting velocities were interpolated along the contour of the detected breakers at time $t+\Delta t$. We discarded all the velocities along the perimeter of the break-

ing fronts that pointed inward towards the interior of the local patch and retained the outward velocities (Sutherland & Melville, 2013). A directional median filter was leveraged to minimize passive foam and outliers. We calculated the median direction of outward velocities per frame, if the median direction is within $\pm 120^o$ of the dominant wave/wind, velocities outside $\pm 120^o$ relative to the median direction are tag passive breakers and discarded. If the median direction opposes the average wind/wave direction, we retain only velocities within $\pm 120^o$ of the average wind/wave direction, similar to Sutherland and Melville (2013). The individual breaking length dl associated with the calculated velocities is the perpendicular distance within the image pixel. The wave-breaking distribution is computed in cartesian space according to

$$\Lambda(c_x, c_y) = \frac{\sum_i \left(dl_i | c_x - \frac{\Delta c_x}{2} \leq c_{x_i} \leq c_x + \frac{\Delta c_x}{2}, c_y - \frac{\Delta c_y}{2} \leq c_{y_i} \leq c_y + \frac{\Delta c_y}{2} \right)}{A_{tot} \Delta c_x \Delta c_y}, \tag{11}$$

where A_{tot} is the total analysis area over all frames, and the bin size $\Delta c_x = \Delta c_y$=0.2 ms^{-1}. The breaking distribution is converted to polar coordinates similar to equation (4)

$$\int \int \Lambda(c_x, c_y)\, dc_x\, dc_y = \int \int \Lambda(c, \theta)\, c\, dc\, d\theta \tag{12}$$

such that the omnidirectional distribution is given by

$$\Lambda(c) = \int_{-\pi}^{\pi} \Lambda(c, \theta)\, c d\theta. \tag{13}$$

Note that the $\Lambda(c)$ framework assumes that breaking fronts propagates with speed c_{br} that is directly proportional to the phase speed of the waves according to $c_{br} = \alpha c$, with $\alpha \approx 0.85$ (Stansell & MacFarlane, 2002; M. L. Banner & Peirson, 2007; Barthelemy et al., 2018; M. Banner et al., 2014). However, for simplicity, α is taken as unity in this analysis. Such that $c_{br} = c$. For comparison against the directional wavenumber spectrum, the velocities are converted to wavenumber via linear dispersion relationship given by

$$c = \sqrt{\frac{g \tanh(kh)}{k}}, \tag{14}$$

where h is the water depth, k is the wavenumber, and g is the acceleration due to gravity. Figure 1b shows a subsampled example of observed wave-breaking fronts.

3 Results

The findings are presented in two subsections. The first subsection analyses the directionality of wave-breaking statistics in terms of $\Lambda(c, \theta)$ and the energy spectrum. In

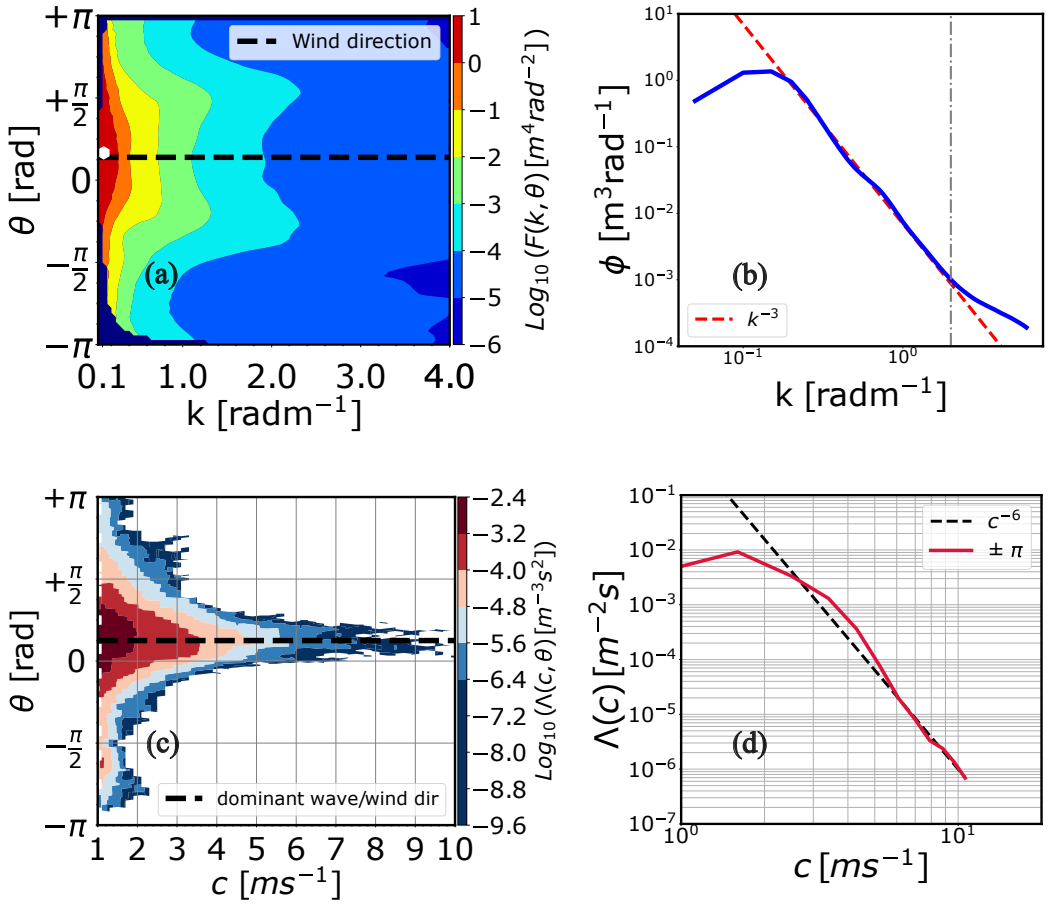

Figure 2. (a) Directional wavenumber spectrum $F(k,\theta)$ and (c) $\Lambda(c,\theta)$ (c) with corresponding azimuth integrated 1-D distributions in (b) and (d), respectively. The k^{-3} line in (b) is the empirical saturation level reported by M. Banner et al. (1989); Romero and Melville (2010a); and Lenain and Melville (2017), and the reference power-law of c^{-6} in (d) corresponds to Phillips (1985) scaling.

the second subsection, the directional spreading of the measured $\Lambda(c,\theta)$ and $F(k,\theta)$ are compared against state-of-the-art spectral models.

3.1 Directional spectrum and breaking statistics

The observed directional spectrum in Figure 2a exhibits bimodality at $k > k_p$. Notice that k_p, marked with a white-hexagon, aligns approximately within 4° of the wind direction. The omnidirectional spectrum $\phi(k) = \int F(k,\theta)k\,d\theta$ is presented in Figure 2b. The tail of the spectrum approximately follows a k^{-3} power-law with a saturation

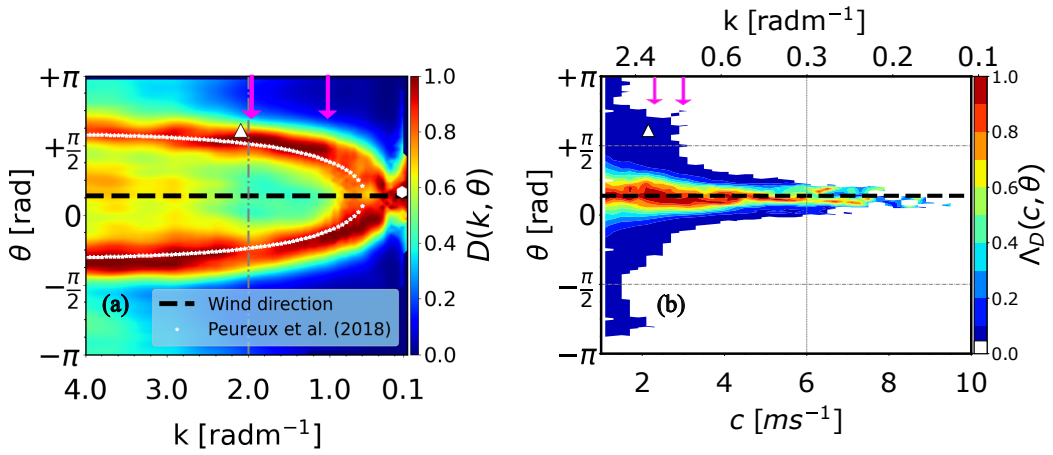

Figure 3. Directional distributions of the energy spectrum $D(k,\theta) = F(k,\theta)/F(k,\theta_{max})$ (a) and breaking statistics $\Lambda_D(k,\theta) = \Lambda(c,\theta)/\Lambda(c,\theta_{max})$ (b). The white stars in (a) represents the empirical parameterization of Peureux et al. (2018) which is given as, $82\sqrt{1-10^{-0.039\left(\frac{k}{k_p}-5\right)}}$. The magenta arrows indicates the wavenumbers at which the cross sections are taken. The white triangle correspond to breaking velocity (and wavenumber) on the upper left corner of the breaker shown in Figure 1.

level $B = \phi(k)k^{-3}$ approximately consistent with airborne lidar measurements (Romero & Melville, 2010a; Lenain & Melville, 2017). Nonetheless, The spectral tail exhibits some noise beyond 2 radm^{-1}, marked by dashed-line in Figures 3a,2b, likely due to camera vibrations noted in section 2.3. Nevertheless, the noise falls outside our analysis range.

Figure 2c shows $\Lambda(c,\theta)$ in polar coordinates for velocities up to 10 ms^{-1}, computed from a total of 20320 images. Among these, 13630 frames contained actively breaking events. There are significantly more slow-moving breakers compared to faster ones. The $\Lambda(c,\theta)$ is unimodal, and the azimuthal width increases towards the lower values of c corresponding to the short waves. In Figures 2d, we show the azimuthally integrated $\Lambda(\mathbf{c})$ (Figure 2c). For reference we show a power-law of c^{-6}. The omnidirectional $\Lambda(c)$ rolls off at $c < 3$ms^{-1}. The roll-off can be attributed to inadequate entrainment of bubbles by the slow (short) waves.

To better visualize the directional distributions of $F(k,\theta)$ and $\Lambda(c,\theta)$, we show them normalized by the scale dependent maxima (I. Young et al., 1995) in Figure 3. Figure 3a more clearly highlights the bimodal behavior of the energy spectrum compared to Fig-

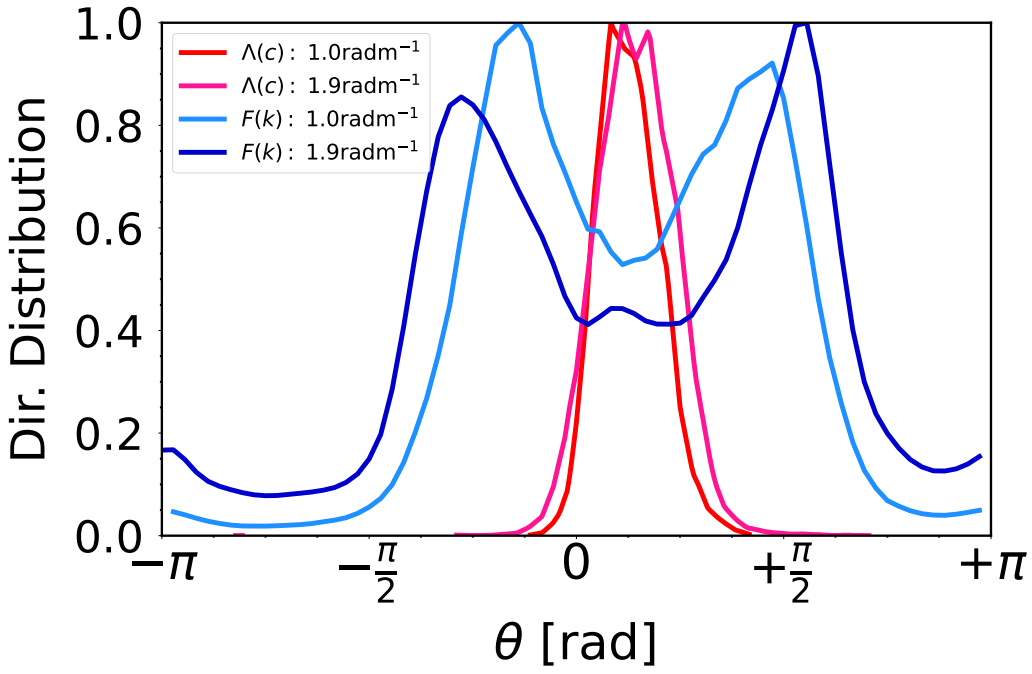

Figure 4. Cross sections of the directional distributions of $\Lambda(c,\theta)$ and the energy spectrum for k = 1.0radm^{-1} and 1.9radm^{-1}.

ure 2a, where it is not normalized. The bimodality approaches $\pm$ 74.9^o in the noise free segment and reaches $\pm$ 80^o for wavenumbers approaching 4 radm^{-1}. Our results are in good agreement with the empirical parameterization by Peureux et al. (2018) for the bimodal maxima as a function of scale shown with white-stars. Similarly, Figure 3b shows the normalized $\Lambda(c,\theta)$, with breakers centered unimodally around the wind/dominant waves across scales. We show direct comparisons of the normalized distributions of $\Lambda(c,\theta)$ and $F(k,\theta)$ in Figure 4 at the two selected scales. The specific wavenumbers are marked by vertical magenta arrows in Figure 3. Interestingly, the $\Lambda(c)$ distribution peaks at the center near the minima of the bimodal energy spectrum. But more importantly, the $\Lambda(c,\theta)$ is much narrower than the spectrum.

3.2 Directional Spreading

In this subsection, we used circular moments to define the directional spreading of the observed $F(k,\theta)$, $\Lambda(c,\theta)$ and the solutions of three spectral wave models implemented in the WAVEWATCH III framework (Tolman et al., 2009). The packages considered in-

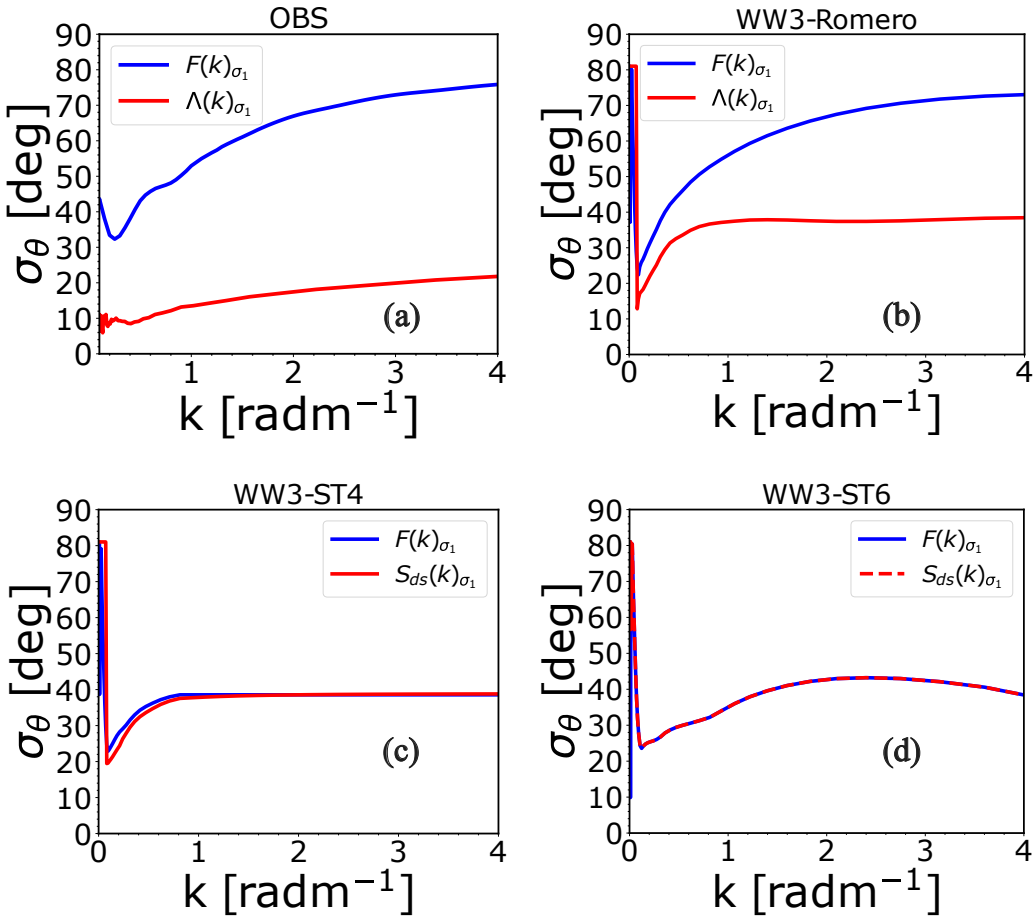

Figure 5. Directional spreading of the energy spectrum (blue) and Λ/S_{ds} for the field measurements (a) and model solutions (b-d), corresponding to Romero (2019), ST4, and ST6, respectively.

clude ST4 (Ardhuin et al., 2010), ST6 (Rogers et al., 2012; Liu et al., 2019; Zieger et al., 2015), and Romero (2019). The solutions used are previously described by Romero and Lubana (2022) and corresponds to idealized time-limited conditions with constant winds of 13 ms^{-1} speed. All solutions were forced with the "exact" computations of the nonlinear resonant four-wave interactions (Tracy & Resio, 1982; van Vledder, 2006). Here we focused on the solutions when the peak period approximately matches that of the field measurements (i.e when the wave age $c_p/U_{10} = 0.8$). The wave breaking parameterization of Romero (2019) is based on Phillips' Λ framework such that the spectral energy dissipation S_{ds} is given by

$$\rho_\omega g S_{ds}(c)dc = \frac{\rho_\omega}{g} b\Lambda(c)c^5 dc, \tag{15}$$

where g is the acceleration due to gravity, ρ_ω is the density of water and b is the strength of breaking parameterized according to Romero et al. (2012). A further simplification of equation (15) gives,

$$S_{ds}(c) = \frac{b}{g^2}\Lambda(c)c^5 \tag{16}$$

or alternatively, $S_{ds}(k) = \frac{b}{g^2}\Lambda(\mathbf{k})c^5$ (Romero, 2019). Due to the unavailability of $\Lambda(\mathbf{k})$ for ST4 and ST6, we used S_{ds} in place of $\Lambda(\mathbf{k})$ in Figure 5c and Figure 5d.

The directional spreading was calculated from the directional moments, which are commonly reported from buoy wave measurements (Kuik et al., 1988), according to

$$\sigma_1(k) = \sqrt{2(1 - \sqrt{{a_1}^2 + {b_1}^2})}, \tag{17}$$

where $a_1(k)$ and $b_1(k)$ are the lowest Fourier coefficients given by

$$a_1(k) = \int_{-\pi}^{\pi} \cos(\theta)\ M(k,\theta)\, k d\theta, \tag{18}$$

and

$$b_1(k) = \int_{-\pi}^{\pi} \sin(\theta) M(k,\theta)\, k d\theta, \tag{19}$$

where $M(k,\theta)$ is the directional distribution

$$M(k,\theta) = \frac{\Upsilon(k,\theta)}{\int_{-\pi}^{\pi}\ \Upsilon(k,\theta)\, k d\theta} \tag{20}$$

with Υ serving as a placeholder for the directional spectrum, Λ or S_{ds}.

The directional spreading of the measured spectrum and $\Lambda(\mathbf{c})$ are shown in Figure 5a. The spreading of the energy spectrum is very broad and well reproduced by the wave breaking parameterization of Romero (2019) as shown in Figure 5b. This is because the dissipation function implemented by Romero (2019) is much narrower than that of the energy spectrum. In contrast, the breaking dissipation of ST4 and ST6 have directional spreadings that are nearly the same (or the same) as the energy spectrum, which results in much narrower energy spectra. In other words, the relatively narrow dissipation of Romero (2019) allows for the nonlinear energy fluxes to broaden the spectrum.

4 Discussion and Conclusions

We presented measurements of wave breaking from visible stereo images. The statistical distribution of wave breaking crest lengths within the Phillips (1985) framework of $\Lambda(c,\theta)$ is unimodal, closely centered around the dominant wave/wind direction and

azimuthally much narrower than the bimodal wave energy spectrum. This is qualitative consistent with the anisotropic Romero (2019) breaking parameterization and solutions. In contrast, the widely used breaking parameterizations with isotropic directional distributions consistently give narrower spectra. For this dataset, the mean angular difference of the directional spreading of the energy spectra produced by the models, shown in Figure 5b,c,d relative to the observed spectrum (Figure 5a) are 2^o, 26^o, 24^o respectively.

The works of Melville et al. (2002), M. Banner et al. (1989),and I. R. Young and Babanin (2006) suggests that shorter (slower) waves are suppressed or 'wiped out' during the passage of actively breaking front(s) leading to smoothening of the sea surface afterwards, this effect, although not yet fully theorized, has been parameterized (Ardhuin et al., 2010), and implemented in several operational wave forecasting models (e.g UK met office, Environment Canada, ECMWF, Meteo France, NCEP). Figures 3 and 4 could be interpreted to further support the aforementioned hypothesis, and such character could possibly be a significant contributor to the bimodal behavior observed in the energy spectrum as the minima of the wave energy bimodality (center region of the spectrum) aligns well with the maxima of the wave breaking distribution. Detailed research will be conducted elsewhere to better understand this relationship. At this stage, one can only speculate that both nonlinear wave-wave interactions and the narrow dissipation due to wave breaking combines together to produce broad bimodal spectrum. The idea is that, wave breaking dissipation through sweeping of shorter waves by big breakers, or long - short wave modulations arising from radiative stress, orbital induced contraction of longer waves which leads to the steeping and eventual breaking of the shorter riding waves could remove energy from the centre region of the directional spectrum while allowing the nonlinearly redistributed energy reaching wider angles to accumulate and grow over time.

The average azimuthal half-width of the measured wave breaking distribution averaged over the entire range of speeds is 25^o. This is slightly narrower compared to Kleiss and Melville (2010) and Gemmrich et al. (2008) who reported a mean spread of 30^o for $\Lambda(\mathbf{c})$. Although the $\Lambda(\mathbf{c})$ distribution is consistently narrow, we did see a few cases when waves break at wide angles. For example, the uppermost portion of the actively breaking front presented in Figure 1 corresponds to the white triangle plotted in Figure 3. Notably, such wide-angle breaking aligns with one of the bimodal lobes of the energy spectrum. While most measurements of $\Lambda(\mathbf{c})$ reported in the literature (including the one

presented here) are azimuthally unimodal, Kleiss and Melville (2010) reported one case with azimuthally bimodal structure at low values of c at short fetches (< 40 km). It is unclear whether the observed bimodality of $\Lambda(\mathbf{c})$ is an artifact due to ensemble averaging over different days or a common feature at low wave ages.

Another important point worth discussing is that our processing of the wave breaking kinematics included both active and passive breakers. Passive breakers can be eliminated by tracking the breakers over time using different criterion, for example the area covered by a breaker should increase with time(Kleiss & Melville, 2011). This was not feasible in our analysis as some intermediate frames were dropped during the camera stabilization exercise. However, we do know that most of the passive breakers are advected back and forth by the orbital velocities at slow speeds. Also our analysis is limited to waves that produce bubbles (Sutherland & Melville, 2013). Future work will target broadband field measurements under a wide range of conditions including misaligned winds and dominant waves to better understand the directionality of wave breaking and the directional energy balance across scales.

5 Availability Statement

The code for detecting and calculating wave-breaking kinematics from visible imagery is available at `https://github.com/akaawase-bernard/WaveBreakingKinematics.git`.

Acknowledgments

The authors are grateful to National Science Foundation for supporting this research (OCE-2319116). L.R. is also supported by NSF grant 2218781. Any opinions, findings, and conclusions or recommendations expressed in this material are those of the author(s) and do not necessarily reflect the views of the National Science Foundation. BA is thankful to the Graduate School, University of Connecticut for the conference travel award, and also express appreciation to Paban Bhuyan and Mackenzie Blanusa for their time and comments during the pre-WISE and Ocean Sciences Meeting presentation sessions. AB is supported by the project PROMETEO (PROtotype of Marine natural Hazard Early-warning sysTem based on Ensemble fOrecasting) funded by the Italian Piano Nazionale di Ripresa e Resilienza (PNRR), CUP B53D23033780001.

References

Alday, M., & Ardhuin, F. (2023). On consistent parameterizations for both dominant wind-waves and spectral tail directionality. *Journal of Geophysical Research: Oceans*, e2022JC019581.

Ardhuin, F., Rogers, E., Babanin, A. V., Filipot, J.-F., Magne, R., Roland, A., ... others (2010). Semiempirical dissipation source functions for ocean waves. part i: Definition, calibration, and validation. *Journal of Physical Oceanography*, *40*(9), 1917–1941.

Banner, M., Barthelemy, X., Fedele, F., Allis, M., Benetazzo, A., Dias, F., & Peirson, W. (2014). Linking reduced breaking crest speeds to unsteady nonlinear water wave group behavior. *Physical review letters*, *112*(11), 114502.

Banner, M., Jones, I. S., & Trinder, J. (1989). Wavenumber spectra of short gravity waves. *Journal of Fluid Mechanics*, *198*, 321–344.

Banner, M., & Young, I. (1994). Modeling spectral dissipation in the evolution of wind waves. part i: Assessment of existing model performance. *Journal of Physical Oceanography*, *24*(7), 1550–1571.

Banner, M. L. (1990). Equilibrium spectra of wind waves. *Journal of Physical Oceanography*, *20*, 966–984. Retrieved from `http://journals.ametsoc.org/doi/abs/10.1175/1520-0485(1990)020%3C0966:ESOWW%3E2.0.CO;2`

Banner, M. L., Babanin, A. V., & Young, I. R. (2000). Breaking probability for dominant waves on the sea surface. *Journal of Physical Oceanography*, *30*(12), 3145–3160.

Banner, M. L., Gemmrich, J. R., & Farmer, D. M. (2002). Multiscale measurements of ocean wave breaking probability. *Journal of Physical Oceanography*, *32*(12), 3364–3375.

Banner, M. L., & Peirson, W. L. (2007). Wave breaking onset and strength for two-dimensional deep-water wave groups. *Journal of Fluid Mechanics*, *585*, 93–115.

Barthelemy, X., Banner, M., Peirson, W., Fedele, F., Allis, M., & Dias, F. (2018). On a unified breaking onset threshold for gravity waves in deep and intermediate depth water. *Journal of Fluid Mechanics*, *841*, 463–488.

Benetazzo, A. (2006). Measurements of short water waves using stereo matched image sequences. *Coastal engineering*, *53*(12), 1013–1032.

Benetazzo, A., Barbariol, F., Bergamasco, F., Torsello, A., Carniel, S., & Sclavo, M. (2016). Stereo wave imaging from moving vessels: Practical use and applications. *Coastal Engineering*, *109*, 114–127.

Benetazzo, A., Bergamasco, F., Yoo, J., Cavaleri, L., Kim, S.-S., Bertotti, L., ... Shim, J.-S. (2018). Characterizing the signature of a spatio-temporal wind wave field. *Ocean Modelling*, *129*, 104–123.

Benetazzo, A., Fedele, F., Gallego, G., Shih, P.-C., & Yezzi, A. (2012). Offshore stereo measurements of gravity waves. *Coastal Engineering*, *64*, 127–138.

Bergamasco, F., Torsello, A., Sclavo, M., Barbariol, F., & Benetazzo, A. (2017). Wass: An open-source pipeline for 3d stereo reconstruction of ocean waves. *Computers & Geosciences*, *107*, 28–36.

Callaghan, A., de Leeuw, G., Cohen, L., & O'Dowd, C. D. (2008). Relationship of oceanic whitecap coverage to wind speed and wind history. *Geophysical Research Letters*, *35*(23).

Deike, L. (2022). Mass transfer at the ocean–atmosphere interface: the role of wave breaking, droplets, and bubbles. *Annual Review of Fluid Mechanics*, *54*, 191–224.

Deike, L., Lenain, L., & Melville, W. K. (2017). Air entrainment by breaking waves. *Geophysical Research Letters*, *44*(8), 3779–3787.

Deike, L., & Melville, W. K. (2018). Gas transfer by breaking waves. *Geophysical Research Letters*, *45*(19), 10–482.

Derakhti, M., Kirby, J. T., Banner, M. L., Grilli, S. T., & Thomson, J. (2020). A unified breaking onset criterion for surface gravity water waves in arbitrary depth. *Journal of Geophysical Research: Oceans*, *125*(7), e2019JC015886.

Donelan, M. A. (2001). A nonlinear dissipation function due to wave breaking. In *Proc. ecmwf workshop on ocean wave forecasting* (pp. 87–94).

Drazen, D. A., Melville, W. K., & Lenain, L. (2008). Inertial scaling of dissipation in unsteady breaking waves. *Journal of fluid mechanics*, *611*, 307–332.

Dulov, V. A., Korinenko, A. E., Kudryavtsev, V. N., & Malinovsky, V. V. (2021). Modulation of wind-wave breaking by long surface waves. *Remote Sensing*, *13*(14), 2825.

Duncan, J. (1981). An experimental investigation of breaking waves produced by a towed hydrofoil. *Proceedings of the Royal Society of London. A. Mathematical*

and Physical Sciences, *377*(1770), 331–348.

Ewans, K. C. (1998). Observations of the directional spectrum of fetch-limited waves. *Journal of Physical Oceanography*, *28*(3), 495–512.

Gemmrich, J. R., Banner, M. L., & Garrett, C. (2008). Spectrally resolved energy dissipation rate and momentum flux of breaking waves. *Journal of Physical Oceanography*, *38*(6), 1296–1312.

Guimarães, P. V. (2018). *Sea surface and energy dissipation* (Unpublished doctoral dissertation). École centrale de Nantes.

Guimarães, P. V., Ardhuin, F., Bergamasco, F., Leckler, F., Filipot, J.-F., Shim, J.-S., ... Benetazzo, A. (2020). A data set of sea surface stereo images to resolve space-time wave fields. *Scientific data*, *7*(1), 145.

Holthuijsen, L. H. (2010). *Waves in oceanic and coastal waters*. Cambridge university press.

Hwang, P. A., Wang, D. W., Walsh, E. J., Krabill, W. B., & Swift, R. N. (2000). Airborne measurements of the wavenumber spectra of ocean surface waves. part i: Spectral slope and dimensionless spectral coefficient. *Journal of physical oceanography*, *30*(11), 2753–2767.

Jasper, A. A., Bernard1a, A. T., & Gudmestad2b, O. T. (2020). Sea state description of asabo offshore in nigeria. *Ocean systems engineering*, *10*(1), 25–47.

Jessup, A., & Phadnis, K. (2005). Measurement of the geometric and kinematic properties of microscale breaking waves from infrared imagery using a piv algorithm. *Measurement Science and Technology*, *16*(10), 1961.

Kleiss, J. M., & Melville, W. K. (2010). Observations of wave breaking kinematics in fetch-limited seas. *Journal of Physical Oceanography*, *40*(12), 2575–2604.

Kleiss, J. M., & Melville, W. K. (2011). The analysis of sea surface imagery for whitecap kinematics. *Journal of Atmospheric and Oceanic Technology*, *28*(2), 219–243.

Kuik, A., Van Vledder, G. P., & Holthuijsen, L. (1988). A method for the routine analysis of pitch-and-roll buoy wave data. *Journal of physical oceanography*, *18*(7), 1020–1034.

Leckler, F., Ardhuin, F., Peureux, C., Benetazzo, A., Bergamasco, F., & Dulov, V. (2015). Analysis and interpretation of frequency–wavenumber spectra of young wind waves. *Journal of Physical Oceanography*, *45*(10), 2484–2496.

Lenain, L., & Melville, W. K. (2017). Measurements of the directional spectrum across the equilibrium saturation ranges of wind-generated surface waves. *Journal of Physical Oceanography*, *47*(8), 2123–2138.

Liu, Q., Rogers, W. E., Babanin, A. V., Young, I. R., Romero, L., Zieger, S., ... Guan, C. (2019). Observation-based source terms in the third-generation wave model wavewatch iii: Updates and verification. *Journal of Physical Oceanography*, *49*(2), 489–517.

Longuet-Higgins, M. (1987). The propagation of short surface waves on longer gravity waves. *Journal of Fluid Mechanics*, *177*, 293–306.

Longuet-Higgins, M., & Stewart, R. (1960). Changes in the form of short gravity waves on long waves and tidal currents. *Journal of Fluid Mechanics*, *8*(4), 565–583.

Longuet-Higgins, M. S. (1976). On the nonlinear transfer of energy in the peak of a gravity-wave spectrum: a simplified model. *Proceedings of the Royal Society of London. A. Mathematical and Physical Sciences*, *347*(1650), 311–328.

Melville, W. K. (1996). The role of surface-wave breaking in air-sea interaction. *Annual review of fluid mechanics*, *28*(1), 279–321.

Melville, W. K., & Matusov, P. (2002). Distribution of breaking waves at the ocean surface. *Nature*, *417*(6884), 58–63.

Melville, W. K., Veron, F., & White, C. J. (2002). The velocity field under breaking waves: coherent structures and turbulence. *Journal of Fluid Mechanics*, *454*, 203–233.

Monahan, E. C., & Muircheartaigh, I. (1980). Optimal power-law description of oceanic whitecap coverage dependence on wind speed. *Journal of Physical Oceanography*, *10*(12), 2094–2099.

Peureux, C., Ardhuin, F., & Guimarães, P. V. (2021). On the unsteady steepening of short gravity waves near the crests of longer waves in the absence of generation or dissipation. *Journal of Geophysical Research: Oceans*, *126*(1), e2020JC016735.

Peureux, C., Benetazzo, A., & Ardhuin, F. (2018). Note on the directional properties of meter-scale gravity waves. *Ocean Science*, *14*(1), 41–52.

Phillips, O. (1985). Spectral and statistical properties of the equilibrium range in wind-generated gravity waves. *Journal of Fluid Mechanics*, *156*, 505–531.

Phillips, O., Posner, F., & Hansen, J. (2001). High range resolution radar measurements of the speed distribution of breaking events in wind-generated ocean waves: Surface impulse and wave energy dissipation rates. *Journal of Physical Oceanography*, *31*(2), 450–460.

Pizzo, N., Deike, L., & Melville, W. K. (2016). Current generation by deep-water breaking waves. *Journal of Fluid Mechanics*, *803*, 275–291.

Rogers, W. E., Babanin, A. V., & Wang, D. W. (2012). Observation-consistent input and whitecapping dissipation in a model for wind-generated surface waves: Description and simple calculations. *Journal of Atmospheric and Oceanic Technology*, *29*(9), 1329–1346.

Romero, L. (2019). Distribution of surface wave breaking fronts. *Geophysical Research Letters*, *46*(17-18), 10463–10474.

Romero, L., Lenain, L., & Melville, W. K. (2017). Observations of surface wave–current interaction. *Journal of Physical Oceanography*, *47*(3), 615–632.

Romero, L., & Lubana, K. (2022). On the bimodality of the wind-wave spectrum: Mean square slopes and azimuthal overlap integral. *Journal of Physical Oceanography*, *52*(7), 1549–1562.

Romero, L., & Melville, W. K. (2010a). Airborne observations of fetch-limited waves in the gulf of tehuantepec. *Journal of Physical Oceanography*, *40*(3), 441–465.

Romero, L., & Melville, W. K. (2010b). Numerical modeling of fetch-limited waves in the gulf of tehuantepec. *Journal of Physical Oceanography*, *40*(3), 466–486.

Romero, L., Melville, W. K., & Kleiss, J. M. (2012). Spectral energy dissipation due to surface wave breaking. *Journal of Physical Oceanography*, *42*(9), 1421–1444.

Romero, L., Ohlmann, J. C., Pallàs-Sanz, E., Statom, N. M., Pérez-Brunius, P., & Maritorena, S. (2019). Coincident observations of dye and drifter relative dispersion over the inner shelf. *Journal of Physical Oceanography*, *49*(9), 2447–2468.

Shin, Y., Deike, L., & Romero, L. (2022). Modulation of bubble-mediated co2 gas transfer due to wave-current interactions. *Geophysical Research Letters*, *49*(22), e2022GL100017.

Stansell, P., & MacFarlane, C. (2002). Experimental investigation of wave breaking criteria based on wave phase speeds. *Journal of physical oceanography*, *32*(5),

1269–1283.

Sutherland, P., & Melville, W. K. (2013). Field measurements and scaling of ocean surface wave-breaking statistics. *Geophysical Research Letters*, *40*(12), 3074–3079.

Thomson, J. (2012). Wave breaking dissipation observed with "swift" drifters. *Journal of Atmospheric and Oceanic Technology*, *29*(12), 1866–1882.

Toffoli, A., Onorato, M., Bitner-Gregersen, E., & Monbaliu, J. (2010). Development of a bimodal structure in ocean wave spectra. *Journal of Geophysical Research: Oceans*, *115*(C3).

Tolman, H. L., et al. (2009). User manual and system documentation of wavewatch iii tm version 3.14. *Technical note, MMAB Contribution*, *276*(220).

Tracy, B. A., & Resio, D. T. (1982). Theory and calculation of the nonlinear energy transfer between sea waves in deep water. In *Proceedings of the army numerical and computers analysis conference* (p. 457).

van Vledder, G. P. (2006). The wrt method for the computation of non-linear four-wave interactions in discrete spectral wave models. *Coastal Engineering*, *53*(2-3), 223–242.

Wu, J., Popinet, S., & Deike, L. (2022). Breaking wave field statistics with a multi-layer numerical framework. *Bulletin of the American Physical Society*.

Young, I. (1995). The determination of confidence limits associated with estimates of the spectral peak frequency. *Ocean engineering*, *22*(7), 669–686.

Young, I., Verhagen, L., & Banner, M. (1995). A note on the bimodal directional spreading of fetch-limited wind waves. *Journal of Geophysical Research: Oceans*, *100*(C1), 773–778.

Young, I. R., & Babanin, A. V. (2006). Spectral distribution of energy dissipation of wind-generated waves due to dominant wave breaking. *Journal of Physical Oceanography*, *36*(3), 376–394.

Zappa, C. J., Banner, M. L., Schultz, H., Gemmrich, J. R., Morison, R. P., LeBel, D. A., & Dickey, T. (2012). An overview of sea state conditions and air-sea fluxes during radyo. *Journal of Geophysical Research: Oceans*, *117*(C7).

Zieger, S., Babanin, A. V., Rogers, W. E., & Young, I. R. (2015). Observation-based source terms in the third-generation wave model wavewatch. *Ocean Modelling*, *96*, 2–25.

Figure 5.

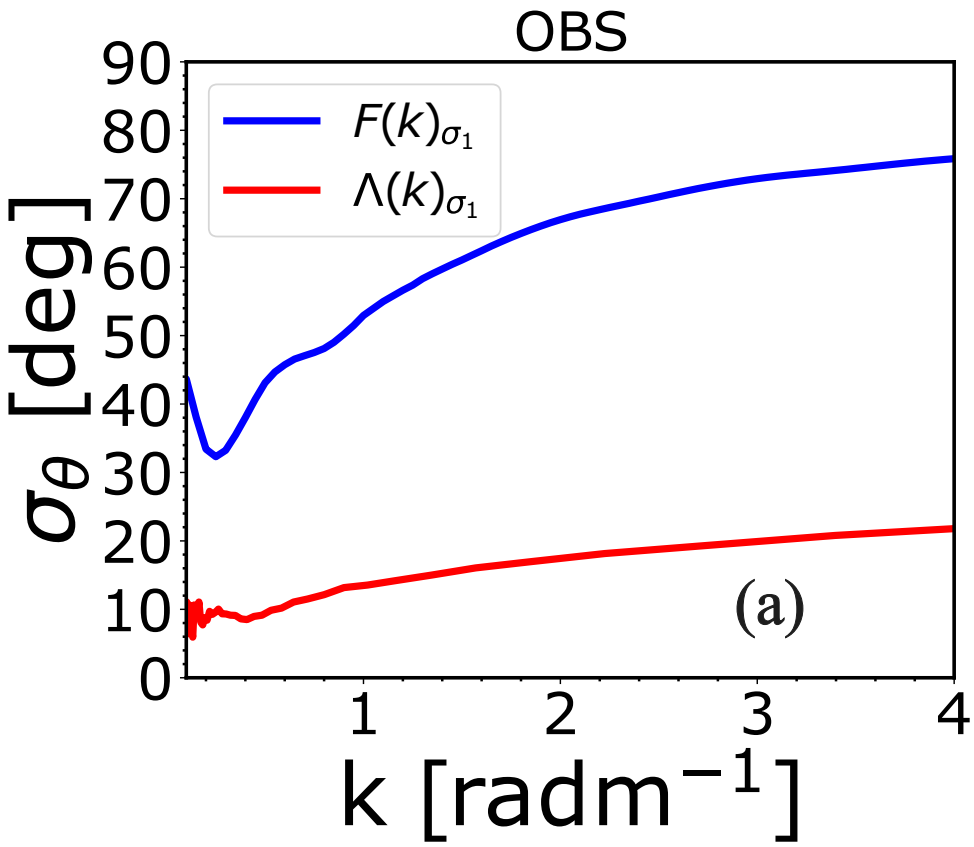
OBS
$F(k)_{\sigma_1}$
$\Lambda(k)_{\sigma_1}$
σ_θ [deg]
k [radm^{-1}]
(a)

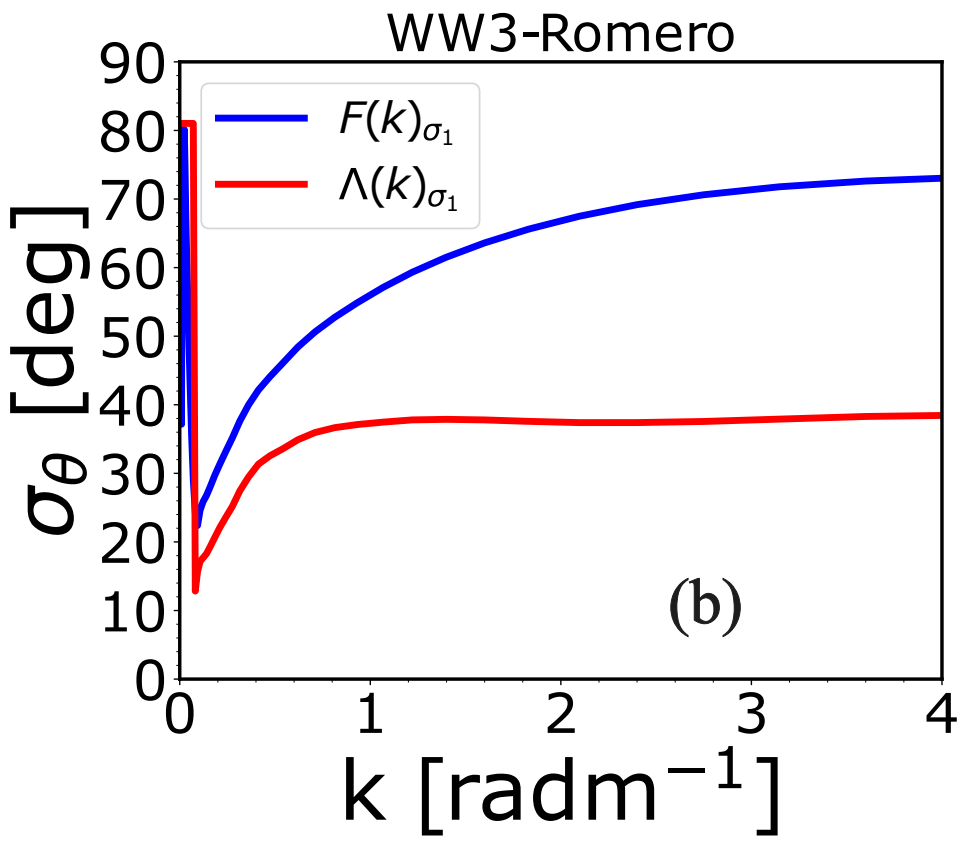
WW3-Romero
$F(k)_{\sigma_1}$
$\Lambda(k)_{\sigma_1}$
σ_θ [deg]
k [radm^{-1}]
(b)

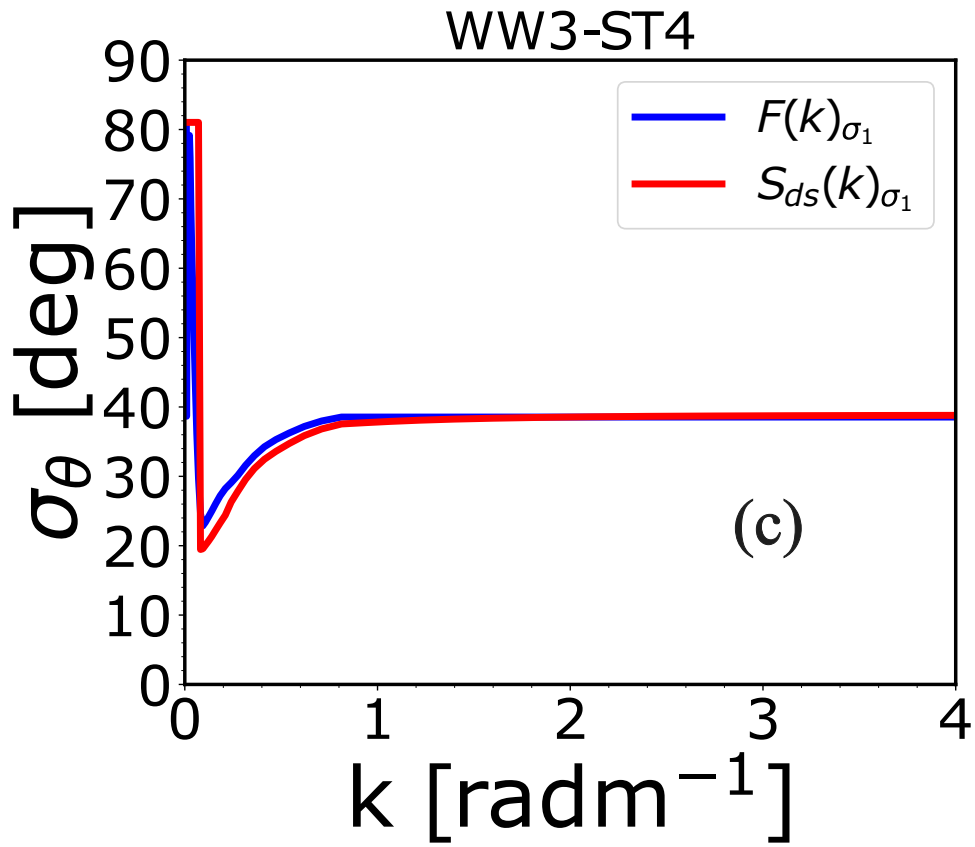
WW3-ST4
$F(k)_{\sigma_1}$
$S_{ds}(k)_{\sigma_1}$
σ_θ [deg]
k [radm^{-1}]
(c)

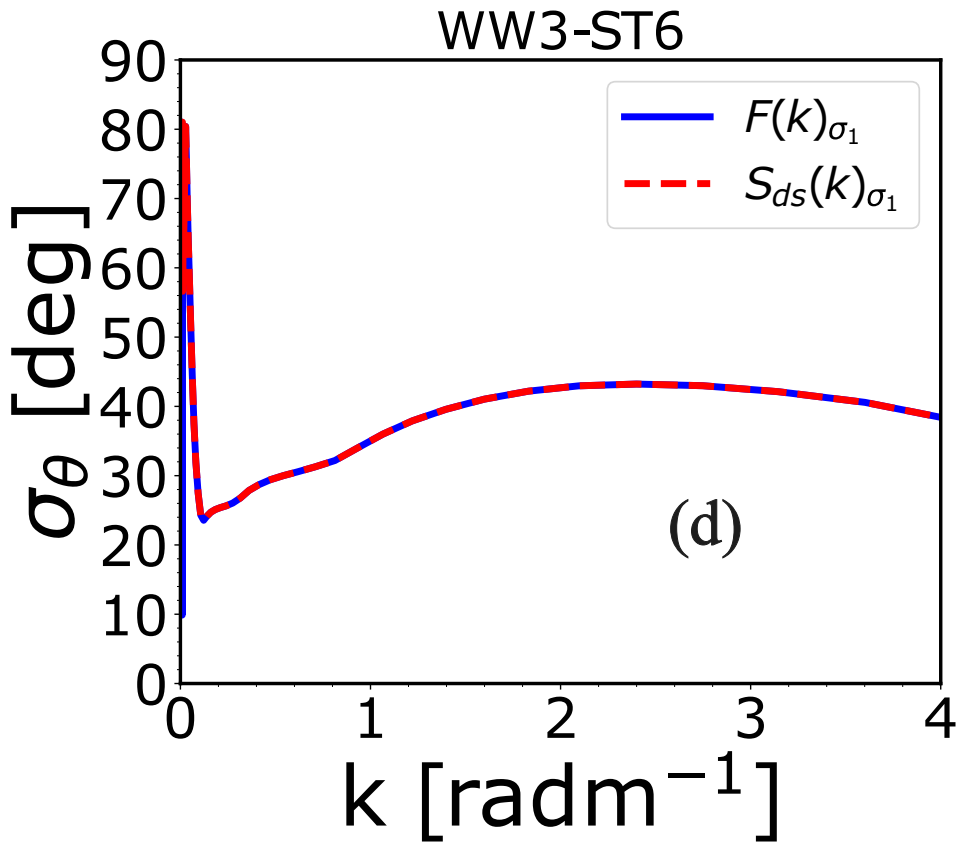
WW3-ST6
$F(k)_{\sigma_1}$
$S_{ds}(k)_{\sigma_1}$
σ_θ [deg]
k [radm^{-1}]
(d)

Figure 4.

Dir. Distribution

1.0
0.8
0.6
0.4
0.2
0.0

$\Lambda(c)$: 1.0radm^{-1}
$\Lambda(c)$: 1.9radm^{-1}
$F(k)$: 1.0radm^{-1}
$F(k)$: 1.9radm^{-1}

$-\pi$ $-\frac{\pi}{2}$ 0 $+\frac{\pi}{2}$ $+\pi$

θ [rad]

Figure 3.

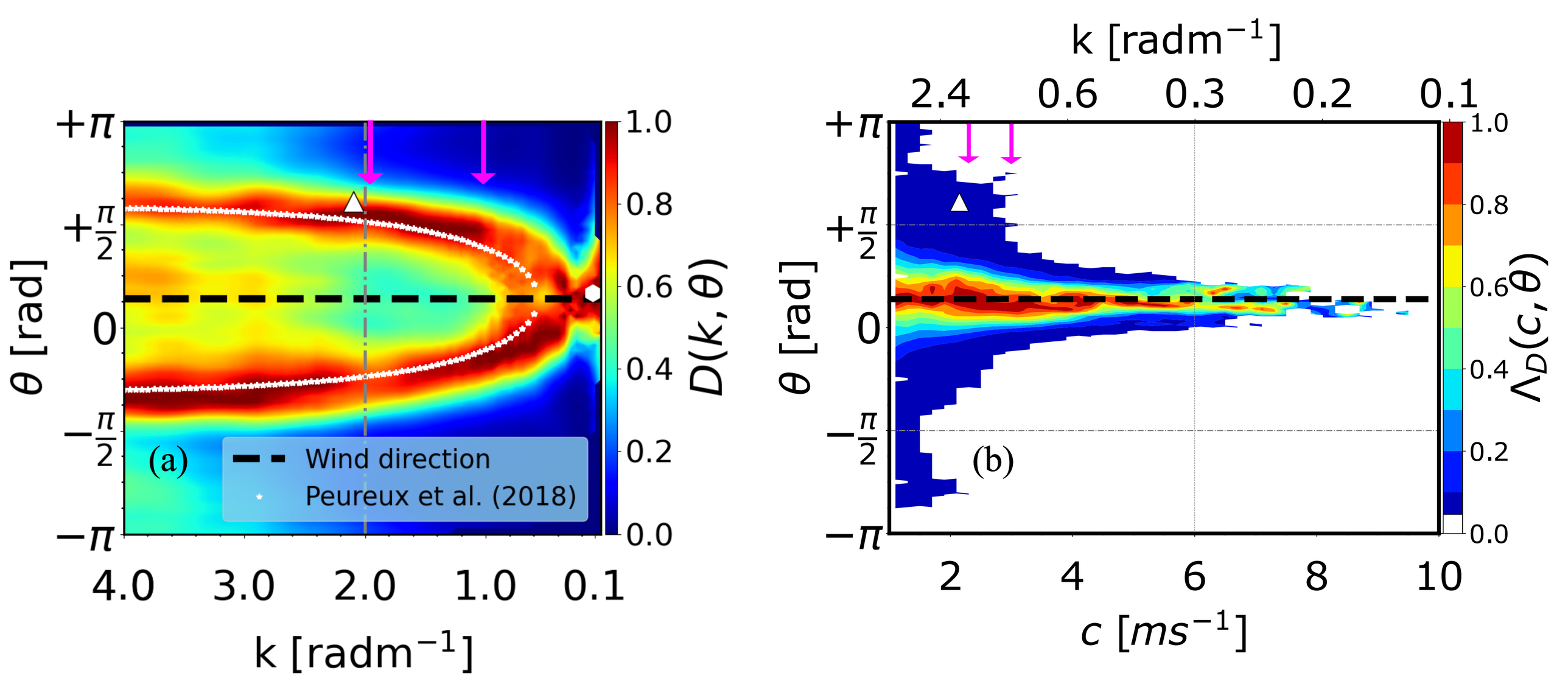
(a)
Wind direction
Peureux et al. (2018)
θ [rad]
+π
+π/2
0
−π/2
−π
4.0
3.0
2.0
1.0
0.1
k [radm^{-1}]
1.0
0.8
0.6
0.4
0.2
0.0
$D(k,\theta)$
(b)
k [radm^{-1}]
2.4
0.6
0.3
0.2
0.1
2
4
6
8
10
c [ms^{-1}]
$\Lambda_D(c,\theta)$

Figure 2.

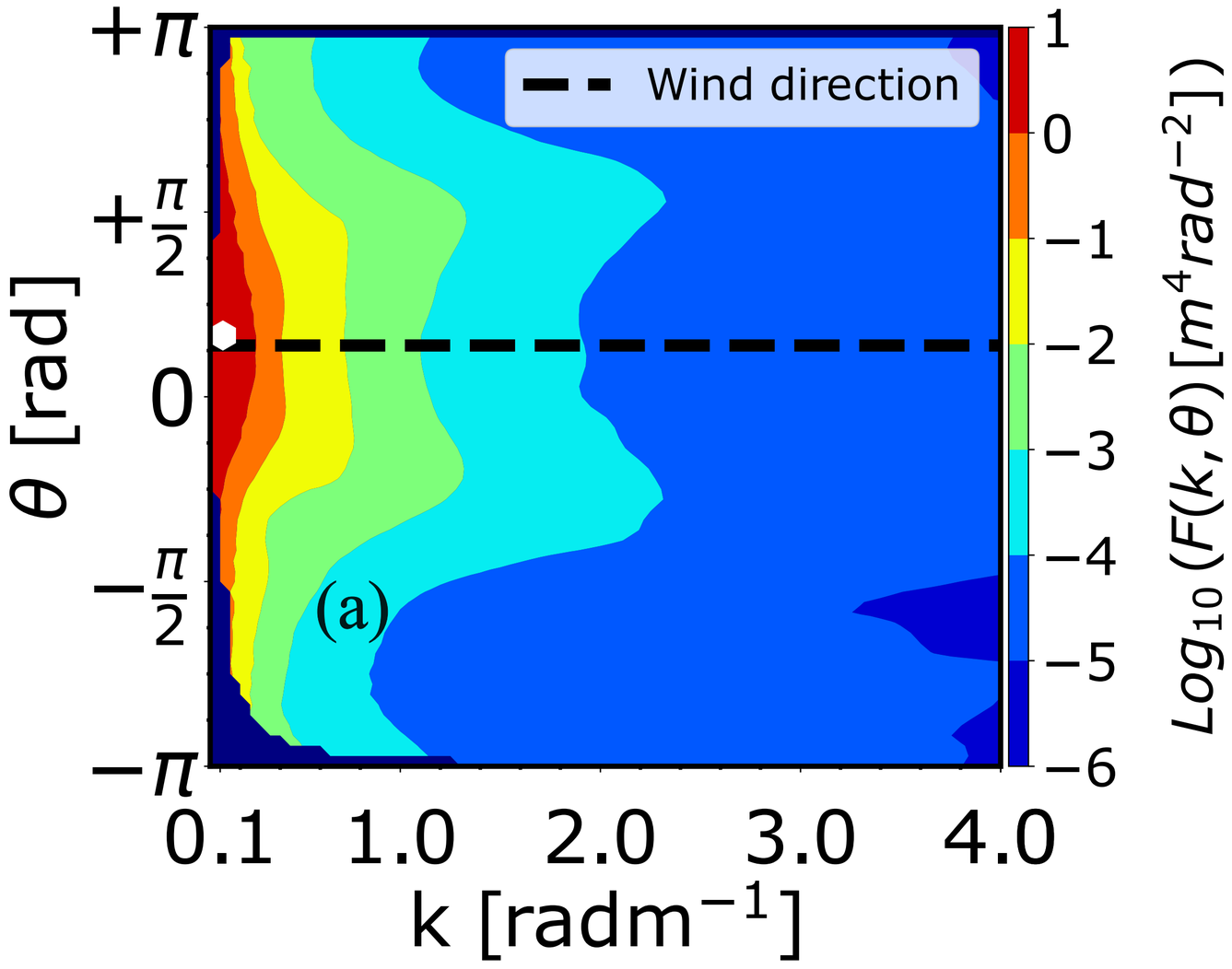
Wind direction
(a)
θ [rad]
+π
+π/2
0
−π/2
−π
k [radm⁻¹]
0.1
1.0
2.0
3.0
4.0
Log₁₀(F(k,θ)[m⁴rad⁻²])
1
0
−1
−2
−3
−4
−5
−6

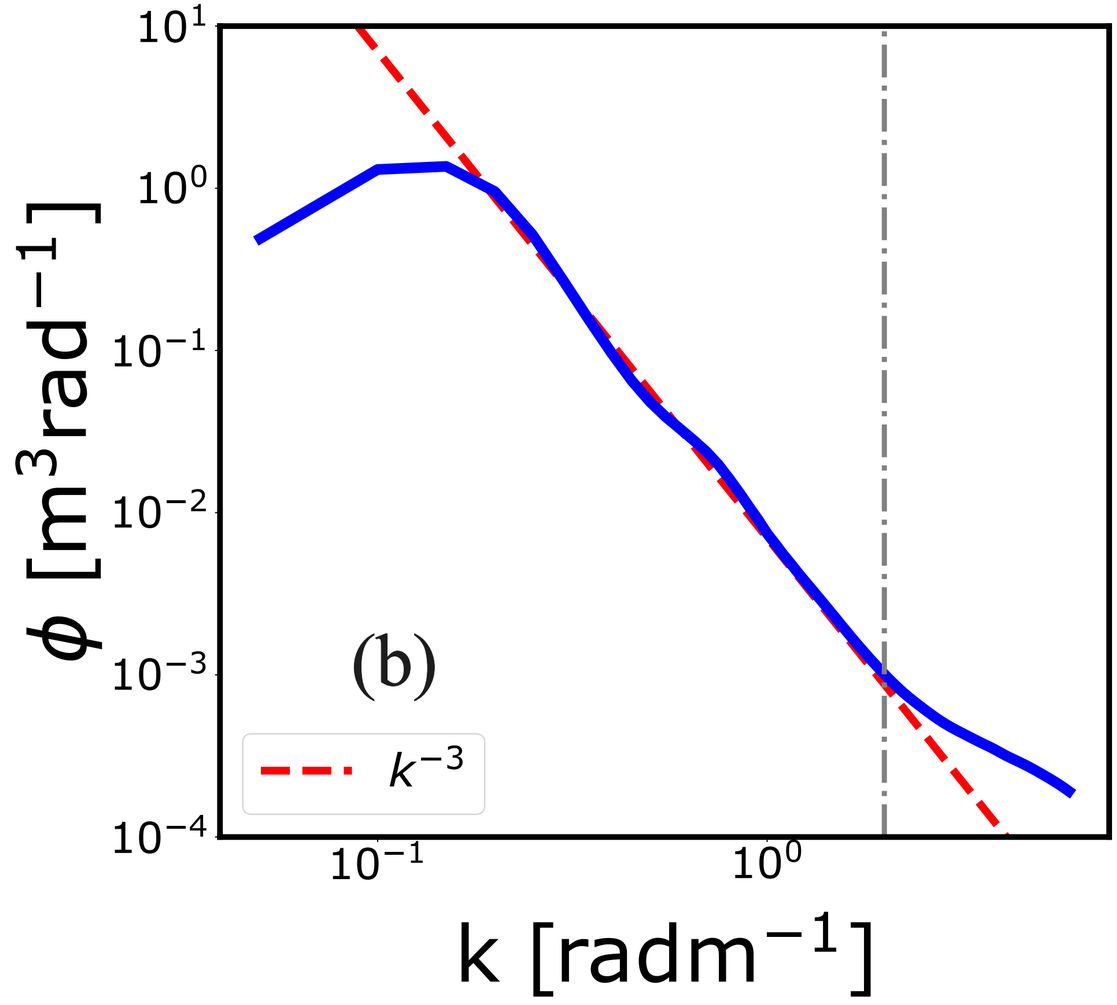
(b)
ϕ [m³rad⁻¹]
10¹
10⁰
10⁻¹
10⁻²
10⁻³
10⁻⁴
k [radm⁻¹]
k⁻³

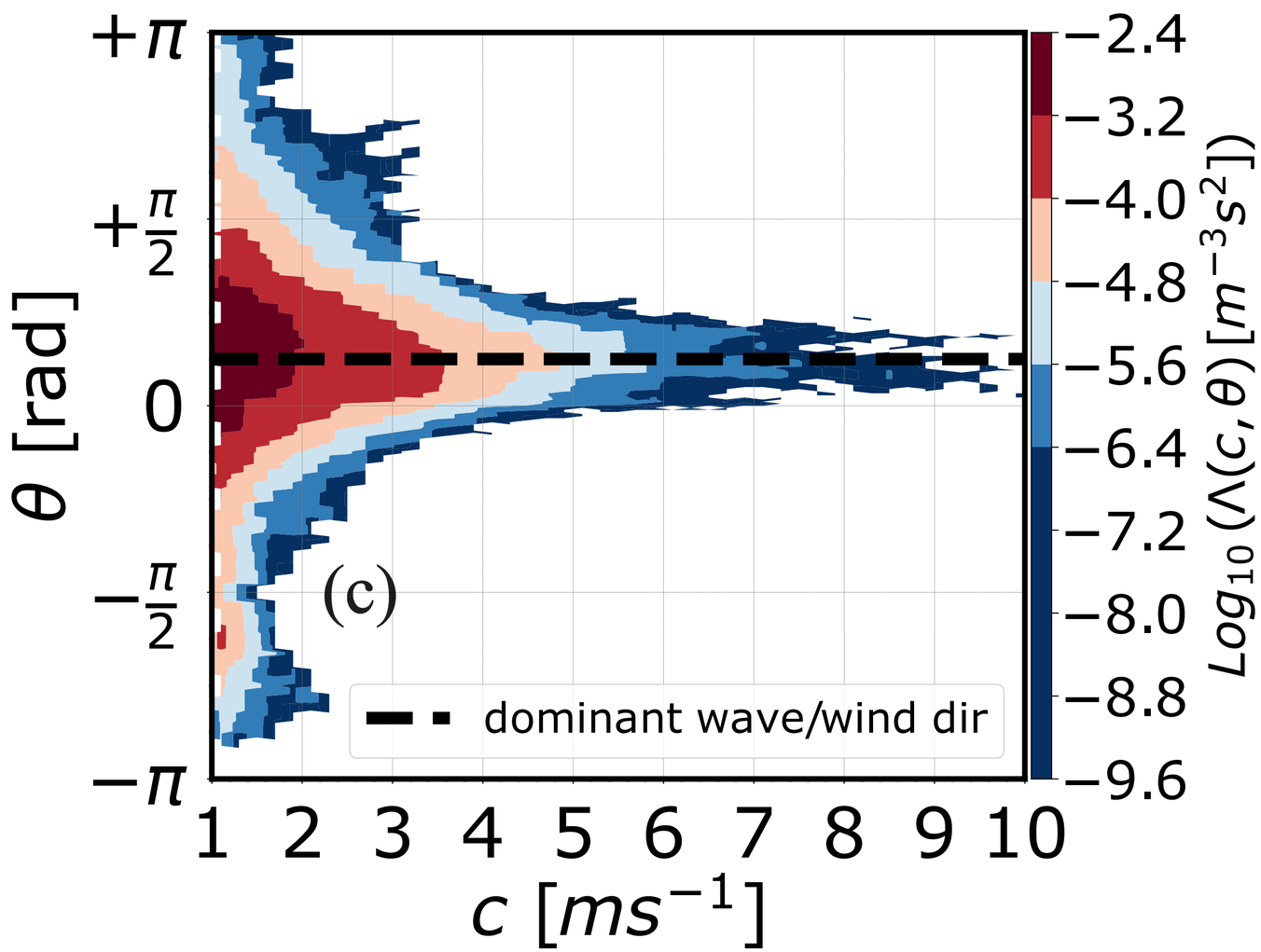
(c)
θ [rad]
+π
+π/2
0
−π/2
−π
c [ms⁻¹]
1
2
3
4
5
6
7
8
9
10
Log₁₀(Λ(c,θ)[m⁻³s²])
−2.4
−3.2
−4.0
−4.8
−5.6
−6.4
−7.2
−8.0
−8.8
−9.6
dominant wave/wind dir

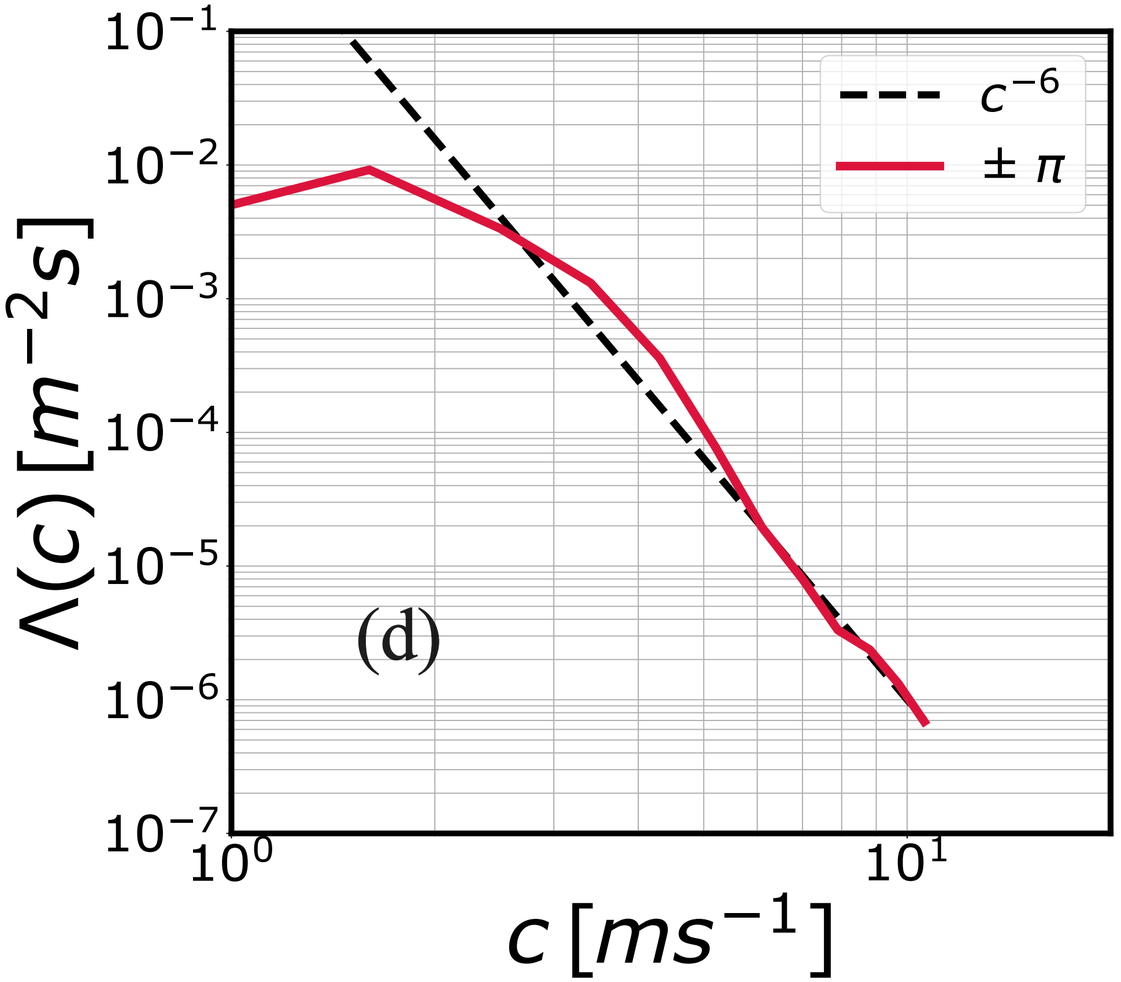
(d)
Λ(c) [m⁻²s]
10⁻¹
10⁻²
10⁻³
10⁻⁴
10⁻⁵
10⁻⁶
10⁻⁷
c [ms⁻¹]
10⁰
10¹
c⁻⁶
± π

Figure 1.

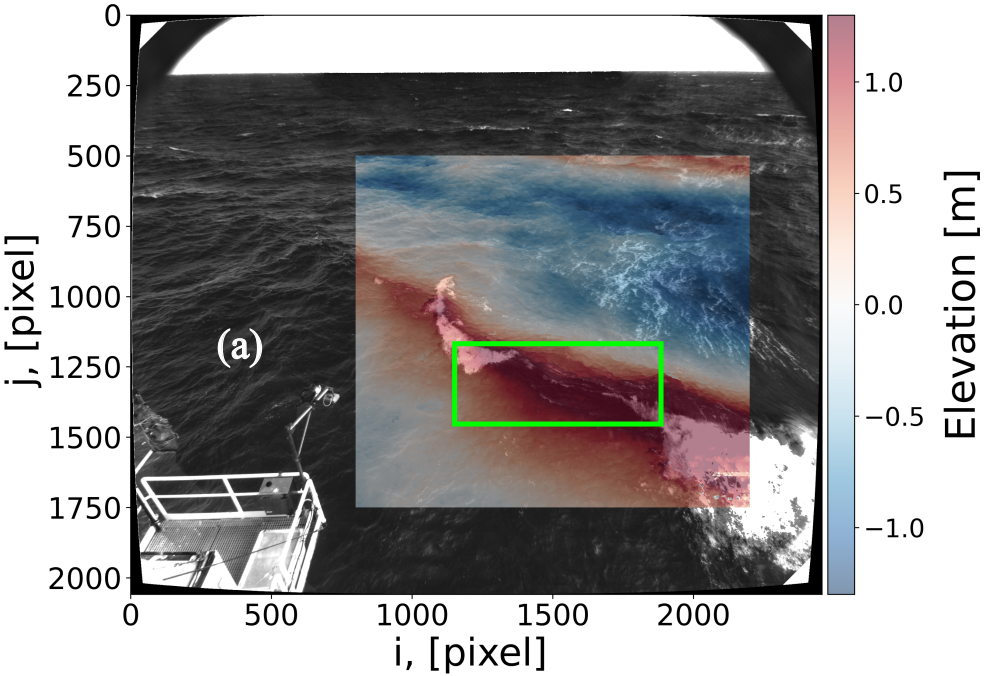
(a)
j, [pixel]
i, [pixel]
Elevation [m]
0
250
500
750
1000
1250
1500
1750
2000
1.0
0.5
0.0
−0.5
−1.0

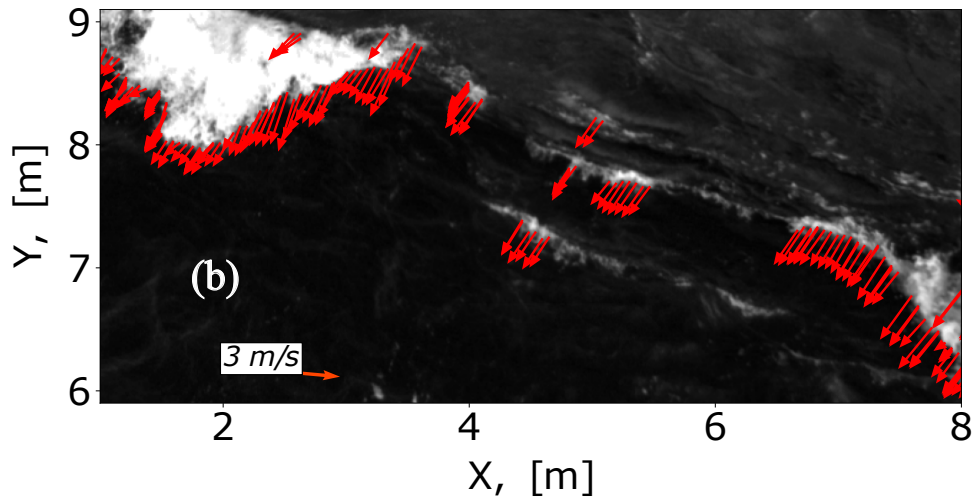
(b)
3 m/s
Y, [m]
X, [m]
9
8
7
6
2
4
6
8